AGU PUBLICATIONS

JGR

Journal of Geophysical Research: Solid Earth

RESEARCH ARTICLE
10.1002/2014JB011738

Special Section:
Stress, Strain and Mass Changes at Volcanoes

Key Points:
- First space strain distribution on Piton de la Fournaise derived from GNSS data
- First model of the Piton de la Fournaise deformation at a large spatial scale
- New insights for the assessment of hazards associated with flank destabilization

Correspondence to:
A. Peltier,
peltier@ipgp.fr

Citation:
Peltier, A., J.-L. Got, N. Villeneuve, P. Boissier, T. Staudacher, V. Ferrazzini, and A. Walpersdorf (2015), Long-term mass transfer at Piton de la Fournaise volcano evidenced by strain distribution derived from GNSS network, *J. Geophys. Res. Solid Earth*, *120*, 1874–1889, doi:10.1002/2014JB011738.

Received 4 NOV 2014
Accepted 30 JAN 2015
Accepted article online 7 FEB 2015
Published online 16 MAR 2015

Long-term mass transfer at Piton de la Fournaise volcano evidenced by strain distribution derived from GNSS network

Aline Peltier[1], Jean-Luc Got[2], Nicolas Villeneuve[1], Patrice Boissier[1], Thomas Staudacher[1], Valérie Ferrazzini[1], and Andrea Walpersdorf[3]

[1]Observatoire Volcanologique du Piton de la Fournaise, IPGP, Sorbonne Paris Cité, UMR 7154 CNRS, Paris, France, [2]ISTerre, CNRS, Université de Savoie, Le Bourget-du-Lac, France, [3]ISTerre, CNRS, Université Joseph Fourier, Grenoble, France

Abstract Basaltic volcanoes are among the largest volcanic edifices on the Earth. These huge volcanoes exhibit rift zones and mobile flanks, revealing specific stress field conditions. In this paper, we present new deformation data issued from the Global Navigation Satellite Systems (GNSS) network installed on Piton de la Fournaise. Density of the GNSS stations allowed us to reach a sufficient resolution to perform a spatially significant analysis of strain at the scale of the active part of the volcano. Since 2007, summit inflation during preeruptive/eruptive sequences (summit extension/cone flanks contraction) alternates with summit deflation during posteruptive/rest periods (summit contraction/cone flanks extension) and generates a "pulsation" of the volcano. This volcano "pulsation" increases rock fracturing and damage, decreases the rock stiffness, and increases the medium permeability. The deformation regime of the mobile eastern flank evidences mass transfer in depth from the summit to the east. During the long-term summit deflation recorded between 2011 and 2014, the upper eastern flank extended steadily eastward whereas the lower eastern flank contracted. Simultaneous extension and eastward displacement of the upper eastern flank and eastward contraction of the middle and lower eastern flank contributes to build the Grandes Pentes relief, steeping the topographic slope. We relate the eastern flank topographic slope spatial variations to rock or basal friction angle changes. The lower flank contraction process is an evidence of its progressive loading by the upper eastern flank, which brings this flank closer to an eventual instability.

1. Introduction

Understanding relief, structure, and dynamics of volcanoes from surface observation, sampling, and measurements is an important and long-lasting task for geoscientists. From this point of view, valuable knowledge may be gained from the study of the very active and large basaltic volcanoes throughout the world. Basaltic volcanoes, like Etna (Italy), Hawaiian volcanoes (USA), and Piton de la Fournaise (La Réunion Island, France), are among the largest volcanic edifices on the Earth. These huge volcanoes exhibit large structures and deformation areas such as rift zones and more or less mobile flanks, which respond to long-lasting stress field conditions due to magmatic processes, gravitational stress, and eventually regional tectonics. Frequently repeated eruptions and intrusions on these volcanoes give insight into these processes. Geological field observations performed on the eroded parts of large basaltic volcanoes [see, e.g., *Walker*, 1986] show that rift zones of these volcanoes are built from the intrusion of thousands of subvertical dikes, a key point for the understanding of how these volcanoes grow. *Dieterich* [1988] investigated carefully the state of stress allowing dike intrusions in such large basaltic volcanoes and show (1) that dike intrusion was favored by basal displacement of the edifice flanks and (2) that the gently steeping slope of the Hawaiian volcanoes were controlled by the basal fault friction coefficient. *Annen et al.* [2001] have considered the injection of 10,000 dikes in a purely elastic volcanic edifice to explain the steep slope of the summit cone of the Piton de la Fournaise edifice. When a purely elastic reaction is considered for the volcanic edifices, such a subvertical intrusion process leads to a high horizontal stress, opposed to the injection process itself. However, observations show that the intrusive process does not stop for long time on these volcanoes. This implies that the average compressive horizontal stress remains very limited to allow for such a long-lasting intrusive process—actually, the horizontal stress needed for creating a dike is tensile. Deformation measurements and seismic tomographies performed on these volcanoes have revealed pressurized magma reservoirs in their edifice. Numerical modeling shows that such pressurized magma reservoirs induce tensile stresses at the

©2015. American Geophysical Union. All Rights Reserved.

summit of the edifice and compressive stresses in the flanks. It favors rock rupture in tension and magma intrusions at the summit and accumulation of compressive elastic stresses in the flanks [see, e.g., *Got et al.*, 2013]. Rock masses are not purely elastic; their strength generally weakens with strain, above some threshold. Accumulation of compressive elastic stresses in the flanks generates a horizontal deviatoric stress. These stresses lead either to the arrest of the eruptive process—when this threshold is not reached—, either to the weakening, strain localization, and eventual rupture of the rock mass at the edifice scale—when this threshold is reached—[see *Carrier et al.*, 2015]. Subhorizontal decollement planes have been identified in the Kilauea southern flank [see, e.g., *Got et al.*, 1994], subhorizontal shear structures have been observed in the eroded parts of the Piton des Neiges volcano (La Réunion Island) [*Famin and Michon*, 2010], and evidences of pressurized subhorizontal structures were found on Piton de la Fournaise [*Got et al.*, 2013; *Chaput et al.*, 2014]. Therefore, vertical magma transfer may be accompanied by horizontal mass transfer following a pattern that appears to be far more complex than those that can be merely modeled using homogeneous linear elastic models.

This horizontal mass transfer may deeply model the flank relief and contribute to flank instabilities. Such flank instabilities may represent major sources of hazard because they can lead to large edifice destabilizations and landslides, one of the most dangerous volcanic phenomena [e.g., *McGuire*, 1996]. It is thus essential to characterize the spatial and temporal evolution of the stress-strain behavior of volcanic edifices to better understand both the causes and the dynamics of the volcano flank deformation and instability.

Improving our knowledge of such processes involves the progressive installation of more and more sophisticated and accurate permanent data acquisition tools. Among those tools, GNSS (Global Navigation Satellite System) receiver networks have an important role as they allow continuous and accurate ground displacement measurements. They are efficient to capture critical events for volcanic process dynamics, which range from incremental deformation to eventually large catastrophic failure. Its accuracy made it currently the most common technique implemented on the field to detect subtle ground displacements associated with volcanic activity. Strain calculation from geodetic data has been extensively used in seismology, tectonics, and glaciology to better evidence fault and crustal pattern, plate spreading, or glacial rebound [e.g., *Arnadottir et al.*, 2009; *Hackl et al.*, 2009; *Takahashi*, 2011] but has been more rarely used in volcano context. In this work we used the permanent GNSS network installed by the Observatoire Volcanologique du Piton de la Fournaise (OVPF).

Piton de la Fournaise is a frequent active basaltic volcano. In 1998, it started a period of high eruptive activity that ended in 2010, during which 34 eruptions occurred [*Roult et al.*, 2012]. In April 2007, the summit of the volcano collapsed during a large distal eruption [e.g., *Michon et al.*, 2007; *Staudacher et al.*, 2009]. Between 2011 and June 2014, the volcano experienced a rest period without any eruptive activity.

Thanks to the progressive densification of the OVPF permanent GNSS network (Figure 1), resolution becomes sufficient to consider a strain study with some spatially significant results. This paper presents a first time-space strain distribution on the whole active part of Piton de la Fournaise during both eruptive and rest periods. Results allow us to investigate the volcano deformation patterns and to draw a first model explaining this deformation at this scale. This provides new insights for the assessment of potential hazards associated with flank destabilization.

2. GNSS Data and Processing

2.1. The Piton de la Fournaise GNSS Network

The recent Piton de la Fournaise GNSS network updates in the frame of national (ANR UnderVolc) [*Brenguier et al.*, 2012] and European (FEDER) projects lead the observatory to currently maintain a permanent GNSS network of 24 stations (against five in 2004 and 13 until end of 2009, see Appendix A). This network is now sufficiently dense to accurately calculate strain tensors with a sufficient space and time resolution. By the end of 2014, ten stations are located on the terminal cone, six on the eastern flank, and eight outside of the Enclos Fouqué caldera (i.e., the structure inside which the terminal cone grows and which extends down to the coastline to the east, see Figure 1 for location). The receivers are Topcon GB1000, Trimble NetRS, and NetR9; they are connected to the observatory by WiFi. The sampling rate of each receiver is one measurement per 30 s.

Daily GNSS solutions have been reprocessed with the GAMIT/GLOBK postprocessing software package [*Herring et al.*, 2010], which uses International GNSS Service (IGS) precise ephemeris, a stable support network

©2015. American Geophysical Union. All Rights Reserved.

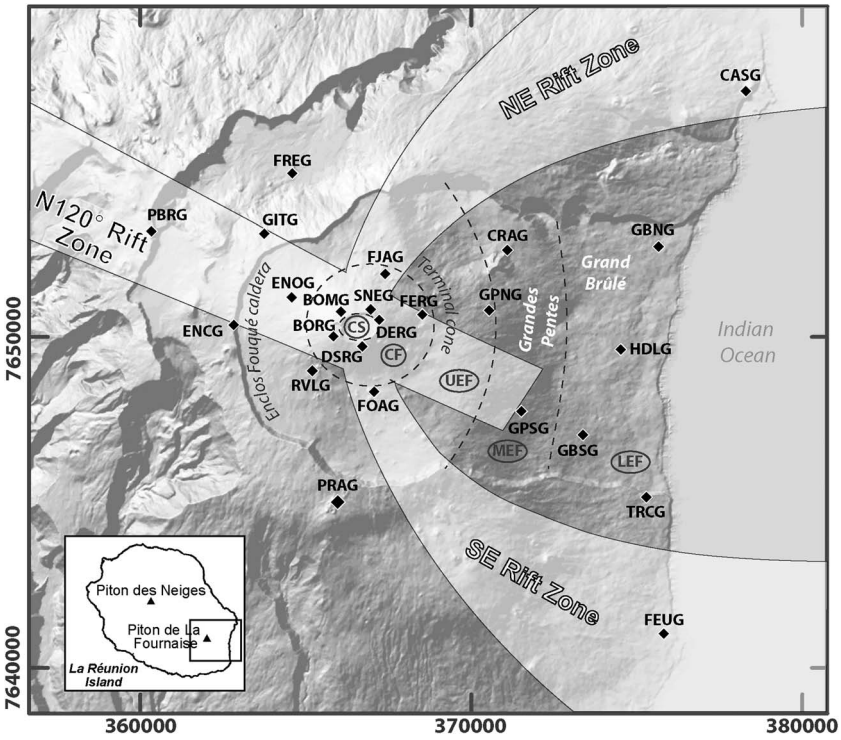


Figure 1. Shaded relief map of the Piton de la Fournaise volcano, with locations of GNSS stations (diamonds), the Enclos Fouqué caldera, the terminal cone, the rift zones, and the Grandes Pentes and Grand Brûlé areas. The CS, CF, UEF, MEF, and LEF initials refer to Cone Summit, Cone Flank, Upper Eastern Flank, Middle Eastern Flank, and Lower Eastern Flank respectively, i.e., the distinct volcano areas we defined and we delimited by dashed contours. The inset shows the location of the volcano on La Réunion Island. Coordinates in UTM WGS84.

of 20 IGS stations around La Réunion Island, a tested parameterization of the troposphere, and models of ocean loading, Earth and lunar tides. Mean horizontal and vertical accuracies are ~0.5 and ~1 cm, respectively. The reprocessing of the whole available GNSS data allows drawing precise time series of ground displacements on the distinct areas of the volcano (Figures 2 and 3, top). The newest FREG, PRAG, PBRG, and FEUG stations have not been used in this study because of their short time series until now (installation late 2012 for FREG and PRAG and early 2013 for PBRG and FEUG, see Appendix A). Ground displacements shown on this paper were corrected from plate motion, deduced from the REUN IGS station located 15 km away from the volcano (see Appendix B).

2.2. Strain Tensor Computation

Our aim is to estimate, as accurately as possible, the strain field at the surface of the volcano. Our study is limited to GNSS displacement data, which implies a spatial sampling of the surface. On Piton de la Fournaise, measured ground displacements are centimetric and occur on kilometric distances during intereruptive periods, i.e., about 10 μstrain, and may reach more than tens of centimeters on kilometric distances during eruptive periods, i.e., about 500 μstrain [e.g., *Peltier et al*., 2008, 2009; *Staudacher and Peltier*, 2015]. But the actual (not measured) strain can locally be far larger, as the largest displacements may be due to rock ruptures and occur on a very short distance. As a consequence, the actual time-space strain field variations may be very heterogeneous.

In this work, as the measured strain remains limited, we will use the linearized first-order approach, based on the small perturbation hypothesis [see, e.g., *Frank*, 1966; *Kahle et al*., 2000; *Hackl et al*., 2009]. In this hypothesis, strain is defined in an infinitesimal way at any point of a continuum: this is the ratio of an infinitely small displacement to the length of an infinitely small vector. Defining completely the state of strain at any point requires two orthogonal vectors in 2-D, and three in 3-D: the complete set of strains defines a tensor. To compute this tensor from the measured displacements we define a unique linear transformation or mapping, *f*, such as the vectors of a given configuration at the time t_2 results from the transformation of the

©2015. American Geophysical Union. All Rights Reserved.

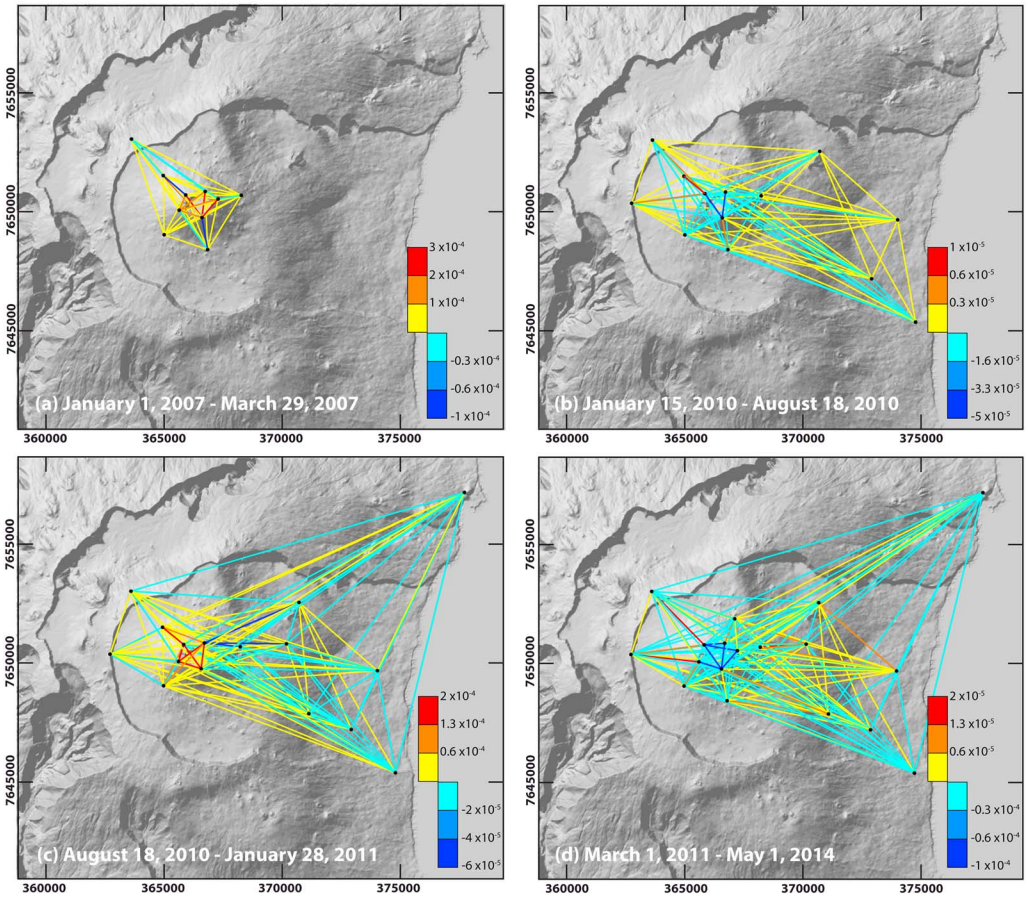


Figure 2. Relative baseline changes for all GNSS station pairs available during representative periods of (a, c) volcano activity and (b, d) rest. Figure 2a period includes one eruption (18 February 2007), and Figure 2c period includes two eruptions (14–31 October and 9–10 December 2010) and two intrusions (19 and 23 September 2010). Coordinates in UTM WGS84.

vectors of another given configuration at the time t_1. In an n-dimension space, let $\mathbf{A_1}$ and $\mathbf{A_2}$ be the matrices formed by the column vectors of the configuration at time t_1 and t_2, respectively. In that case,

$$A_2 = FA_1 \tag{1}$$

where **F** is the transformation gradient tensor.

Therefore,

$$F = A_2 {A_1}^{-1} \tag{2}$$

The f linear transformation is completely characterized by the computation of the **F** tensor and of the average translation. Both of them do not depend on the position: the transformation is thus homogeneous. In equation (2) the inversion of $\mathbf{A_1}$ shows that when vectors used in $\mathbf{A_1}$ are too close to colinearity, condition number may be large, and increasing the variance in the estimation of **F**. Displacement **D** may be easily computed from F:

$$D = (F - I)V \tag{3}$$

where **I** is the identity matrix and **V** is a vector, both in an n-dimension space.

The tensor

$$G = F - I \tag{4}$$

is the gradient of displacement. It may be decomposed into an antisymmetric part, containing the information on rotation, and a symmetric part, containing the internal strain, represented by the strain tensor $\boldsymbol{\varepsilon}$:

$$G = \frac{G + G^T}{2} \tag{5}$$

©2015. American Geophysical Union. All Rights Reserved.

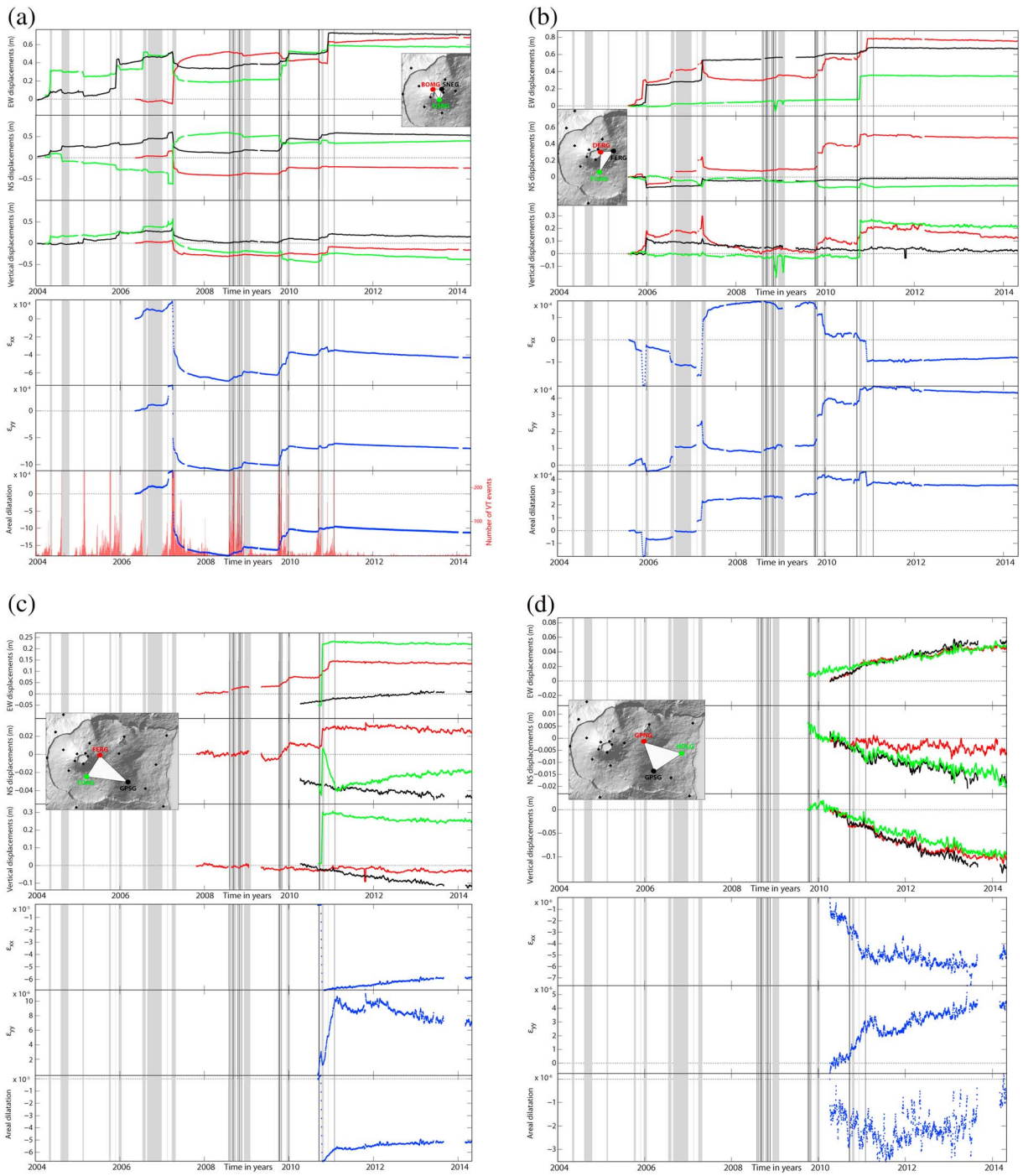


Figure 3. Cumulated displacements (with plate motion removed) and total longitudinal strains ε_{xx} ε_{yy} calculated from five representative triangles: (a) the cone summit (BOMG, SNEG, DSRG), (b) the cone flank (DERG, FERG, FOAG), (c) the upper eastern flank (FOAG, FERG, GPSG), (d) the middle eastern flank (GPSG, GPNG, HDLG), and (e) the lower eastern flank (GPSG, GPNG, HDLG). (top) Cumulated displacements recorded on the EW, NS, and vertical components of the GNSS stations (colors refer to the GNSS defining the triangle and represented in the inset). (bottom) Total longitudinal strains ε_{xx} and ε_{yy} and the areal dilatation inside the corresponding triangle. Grey areas and black vertical lines represent timing of eruptions and intrusions, respectively. On Figure 3a, the red histograms represent the number of volcano tectonic earthquakes recorded below the summit per day. In order to have longer time series, we merged the trends of BOMG with the ones of the old station BONG, only 103 m away (Figure 3a), and the trends of FOAG with the ones of the old station FORG, only 23 m away (Figure 3b).

©2015. American Geophysical Union. All Rights Reserved.

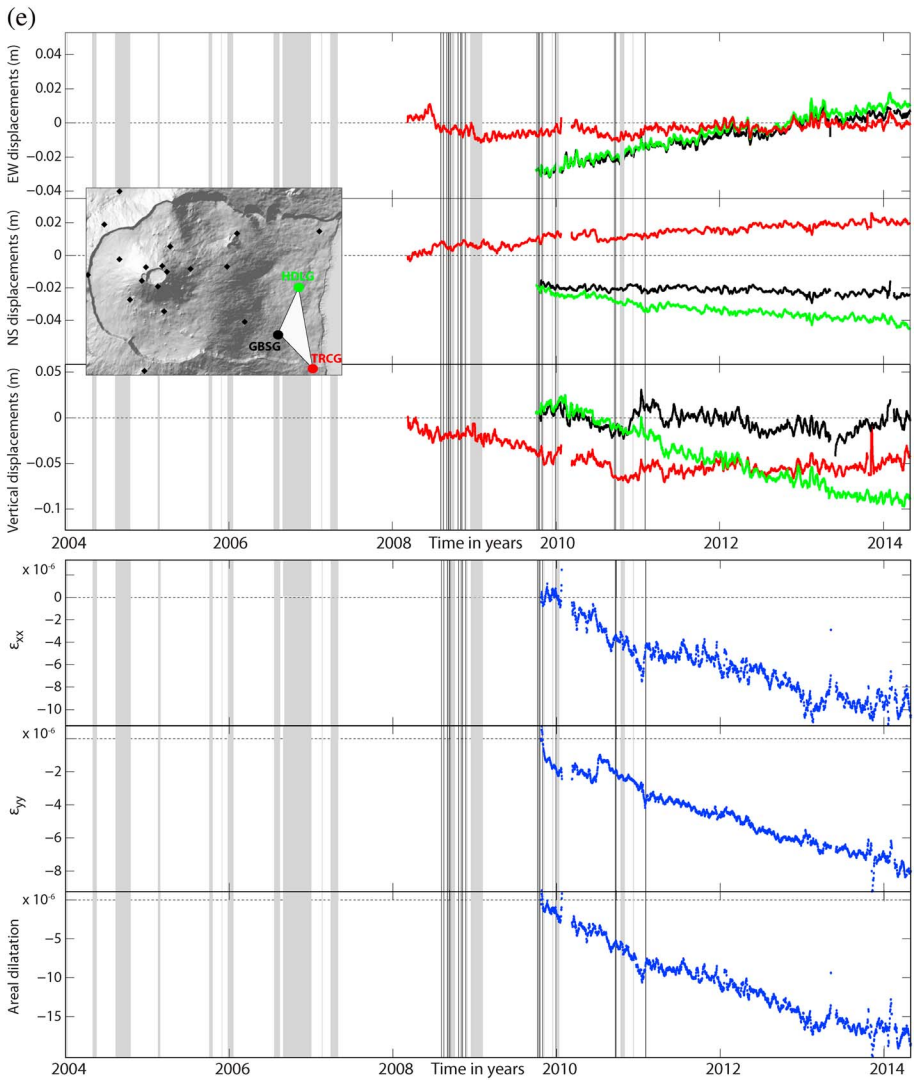


Figure 3. (continued)

The parameter $\boldsymbol{\varepsilon}$ is the tensor of small strains; this is the linearized form of the Green-Lagrange tensor.

Eigenvectors and eigenvalues of $\boldsymbol{\varepsilon}$ are respectively the direction and the module of the principal strains.

Though the measured average strain may be considered as small, this strain is computed from vectors that are not infinitesimal. They define domains for which strain is supposed to be constant, which is not true. The question of the pertinent scale for sampling the strain field may be theoretically answered by using Shannon's theorem: the maximal characteristic dimension of each domain has to be lower than the half minimal spatial wavelength of the (a priori unknown) displacement spectra. In practice, only the dominant wavelengths of the strain field may be inferred from the measured displacements and our a priori mechanical knowledge of the deformation process. Displacements decrease with distance to the pressure center, so that the strain field has higher frequencies along the radial direction than along the tangential direction. Therefore, for a given station distribution, undersampling will be limited when using domains that are elongated tangentially rather than radially. In a general manner, we have tried to design a mesh for which strain was as homogeneous as possible in each domain, with angles between adjacent vectors that warrant the stability of the computation. Translation carries the information brought by strain at wavelengths larger than the characteristic dimension of each domain.

Deformation of the volcano is a 3-D process; however, displacements are measured at the surface, with GNSS stations that may be used to form kilometric-scale triangles or tetrahedrons (for respectively 2-D or 3-D strain

©2015. American Geophysical Union. All Rights Reserved.

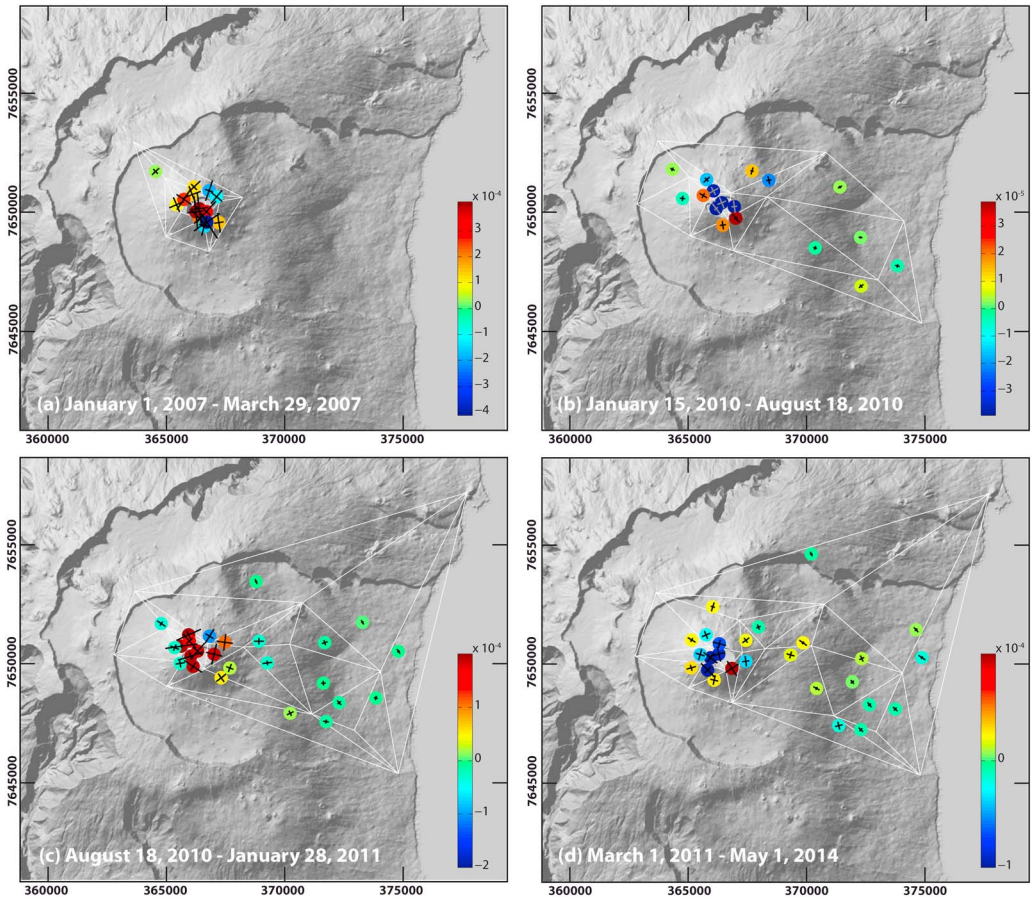


Figure 4. Major principal strain ε_1 spatial distribution (in color) during representative periods of (a, c) activity and (b, d) rest. Figure 4a period includes one eruption (18 February 2007), and Figure 4c period includes two eruptions (14–31 October and 9–10 December 2010) and two intrusions (19 and 23 September 2010). Black crosses represent the orientation of the principal strains. The center of each solid colored circle is the weighted geometric center of the corresponding triangle, the weight being the module of the horizontal displacement recorded at each station. Coordinates in UTM WGS84.

analysis). At this scale, the vertical range of GNSS stations is limited, and using flat tetrahedrons is not convenient for estimating a stable vertical strain. Moreover, the computed vertical strain is internal to each tetrahedron, and most of the information on the vertical deformation process is locally carried by the vertical translation, as there is no displacement measurement performed at depth. Finally, sampling the surface with a triangular mesh rather than a tetrahedral one provides an improved spatial resolution. For these reasons, we chose to compute 2-D strain tensor and use triangular meshing. For each triangle, we compute the average translation and the internal strain tensor for distinct representative periods and display ε_1 and ε_{xx} on map views (Figures 4 and 5). We chose to represent the spatial strain distribution both by the first principal strain ε_1 but also by the strain in the E-W direction, ε_{xx}, as the direction of the eastern lateral spreading is about E-W [e.g., *Clarke et al*., 2013; *Brenguier et al*., 2012; *Staudacher and Peltier*, 2015].

Computing incremental strain between two consecutive displacement measurements with a daily sampling rate faces the problem of cumulating the 0.5 cm horizontal and 1 cm vertical measurement noise, whereas displacements are differentiated and time changes are often less than the standard deviation measurement. Reducing noise to compute a significant strain over the whole time series would involve a moving time average with a ~10 day averaging width, which introduces a strong bias during preeruptive and eruptive periods. Moreover, total strain is more easily interpretable than the incremental one and remains small, respecting the small perturbation hypothesis. For these reasons, we choose to compute the strain as a function of time with respect to a unique time reference, chosen as the first available GNSS measurement common to the triangle stations. We thus obtained the total strain on the whole available period (Figure 3,

©2015. American Geophysical Union. All Rights Reserved.

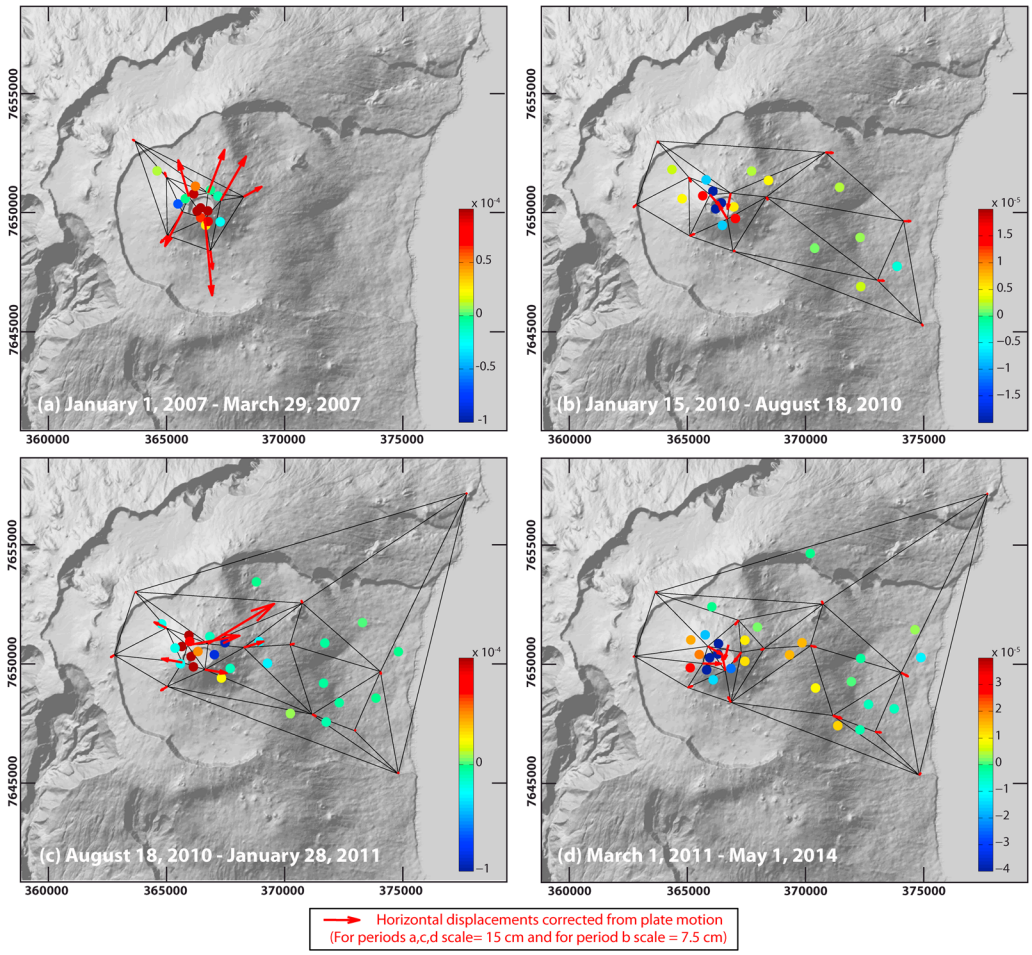


Figure 5. Longitudinal strain ε_{xx} spatial distribution (in color) during representative periods of (a, c) activity and (b, d) rest. Red vectors represent the corresponding horizontal displacements recorded at the GNSS stations (with plate motion removed). Figure 5a period includes one eruption (18 February 2007), and Figure 5c period includes two eruptions (14–31 October and 9–10 December 2010) and two intrusions (19 and 23 September 2010). The center of each solid colored circle is the weighted geometric center of the corresponding triangle, the weight being the module of the horizontal displacement recorded at each station. Coordinates in UTM WGS84.

bottom). Moving time averages were performed on displacement data with a 3 day interval, a good bias variance compromise that enhances stability in the strain tensor computation while keeping high frequencies in the resulting time series.

3. Results

Figure 2 shows the relative baseline changes for all GNSS station pairs available during two periods representative of the volcano high eruptive activity (pre-2007 summit collapse eruptive activity, Figure 2a; and post-2007 summit collapse eruptive activity, Figure 2c) and two others representative of volcano rest (Figures 2b and 2d). Except for the pre-2007 summit collapse period, we chose the longest periods during which the largest number of GNSS stations was available. We calculated the relative baseline changes as $\Delta l(t)/l(t_o)$, where $\Delta l(t)$ is the baseline length variation between the times t and t_0 and $l(t_o)$ is the baseline length at t_0. The main ground displacements occurred at the summit with an alternation between inflation and deflation periods directly linked with periods of activity and rest, respectively. Periods including eruptive activity are characterized by lengthening of baseline distances at the summit (Figures 2a and 2c) and shortening of baseline distances on the cone flanks; whereas the reverse is observed during rest periods (Figures 2b and 2d). Figures 4 and 5 represent the spatial distribution of ε_1 and ε_{xx}, respectively, during the same four periods defined above. As observed with the baseline maps, the strain intensity (ε_1 ε_{xx}) is maximal in the summit area (with ε_1 up to 10^{-3}). According

©2015. American Geophysical Union. All Rights Reserved.

to the volcano deformation pattern, we distinguished five domains on the volcano: (1) the Cone Summit, CS; (2) the Cone Flank, CF; (3) the Upper Eastern Flank, UEF; (4) the Middle Eastern Flank, MEF; and (5) the Lower Eastern Flank, LEF (see their location on Figure 1). For these five domains, we represent the time evolution of the cumulated displacements (with plate motion removed), the total longitudinal (or linear) strains ε_{xx}, ε_{yy}, and the areal dilatation ($\varepsilon_{xx}+\varepsilon_{yy}$) inside triangles representative of these domains (Figures 3a–3e).

3.1. Deformation of the Terminal Cone

As previously observed [e.g., *Peltier et al*., 2008, 2009; *Staudacher and Peltier*, 2015], the volcano, and especially its summit, deforms on two time scales, at long-term and slow rates during intereruptive periods and at short-term and rapid rates during eruptive/intrusive periods (Figure 3).

The strongest displacements (up to a few tens of centimeters per hour) are associated to eruptive/intrusive activity (Figures 2a, 2c, 3a, and 3b, top); the signs of the horizontal displacement depending on the dike paths at depth [e.g., *Peltier et al*., 2009; *Staudacher and Peltier*, 2015]. These displacements start usually with the most intensive phase of the preeruptive or intrusive seismic crises characterized by numerous merged events (more than six earthquakes per minute) located above sea level below the summit and of magnitudes up to 2.5 [*Roult et al*., 2012].

In April 2007, a major event in the volcano history occurred; the Dolomieu crater collapsed on a depth of about 340 m [e.g., *Michon et al*., 2007; *Staudacher et al*., 2009] during the most voluminous eruption monitored by the observatory (about 220 Mm^3 of lava flows have been emitted; i.e., 10 to 100 times more than a typical eruption on this volcano) [*Roult et al*., 2012]. These concomitant events were accompanied by a strong summit contraction (e.g., areal dilatation of $\sim -18\cdot10^{-4}$ with $\varepsilon_{xx}=\sim -6\cdot10^{-4}$ and $\varepsilon_{yy}=\sim -12\cdot10^{-4}$ inside the BOMG-SNEG-DSRG triangle; Figure 3a, bottom) and an EW extension of the cone flank (e.g., $\varepsilon_{xx}=\sim 2.5\cdot10^{-4}$ inside the DERG, FERG, FOAG triangle; Figure 3b, bottom). The ε_{xx} antagonist behavior on these two areas pursued with an exponential decreasing rate until the repressurization of the plumbing system preceding a few weeks the renewal of the eruptive activity in September 2008. The rate of the summit deflation was estimated at 0.5 m/yr on SNEG station during the April 2007 events and it then decreased exponentially, up to ~0.05 m/yr in mid-2008 (Figure 3a, top) [*Peltier et al*., 2010; *Rivet et al*., 2014; *Staudacher and Peltier*, 2015].

During the resumptions of the eruptive activity (middle to end of 2008, end of 2009, and end of 2010), the trends reversed, with a strain increase at the summit (extension) and a strain decrease on the cone flanks (contraction), accompanied by a rotation of θ_1 (Figures 3a, 3b, bottom 4c, and 5c).

After each eruptive period of 2008, 2009, and 2010, the slow-rate summit deflation observed after the April 2007 events renewed, as observed during the longest intereruptive/rest periods, which occurred early to middle of 2009, early to middle of 2010, and after the 2 February 2011 intrusion. By contrast, before April 2007, mainly slow-rate long-term inflation (0.01 to 0.25 m/yr on SNEG station) [*Peltier et al*., 2008, 2009] was observed during intereruptive periods and was interpreted by a continuous refilling of the shallow plumbing system (Figure 3a, top) [*Peltier et al*., 2009].

The alternation between summit inflation and summit deflation clearly appears on Figure 3a (top); the NS components of the BOMG and SNEG stations, on the one hand, and the DSRG station, on the other hand, diametrically opposed relative to the surface trace of the pressure center, show clear antiphase trends over time, getting closer and away during deflation and inflation periods, respectively.

3.2. Deformation of the Eastern Flank

Since the implementation of GNSS receivers in the eastern flank of the volcano in 2009–2010, deformation pattern outside of the terminal cone has been progressively better characterized both during rest and eruptive periods. Since their installation, stations GBNG, CRAG (northern part of the Grandes Pentes and Grand Brulé areas; Figure 1), and TRCG (just outside of the southeastern part of the Enclos Fouqué caldera) did not record any significant ground motion (Figure 6). The other stations (GPSG, GPNG, GBSG, and HDLG) evidenced an eastward motion of the eastern flank (up to ~0.02 m/yr) accompanied by a continuous subsidence (up to ~0.025 m/yr; Figures 3d, 3e, top, and 6) [*Brenguier et al*., 2012; *Peltier et al*., 2015; *Staudacher and Peltier*, 2015]. Among these four stations, the subsidence recorded on GPNG, GPSG, and HDLG is greater than their eastern motion. Only the GBSG station did not record any significant vertical motion. GPNG, GPSG, and HDLG stations are installed on relatively young lava flows (2004 for GPNG, 2001 for HDLG, and 2000

©2015. American Geophysical Union. All Rights Reserved.

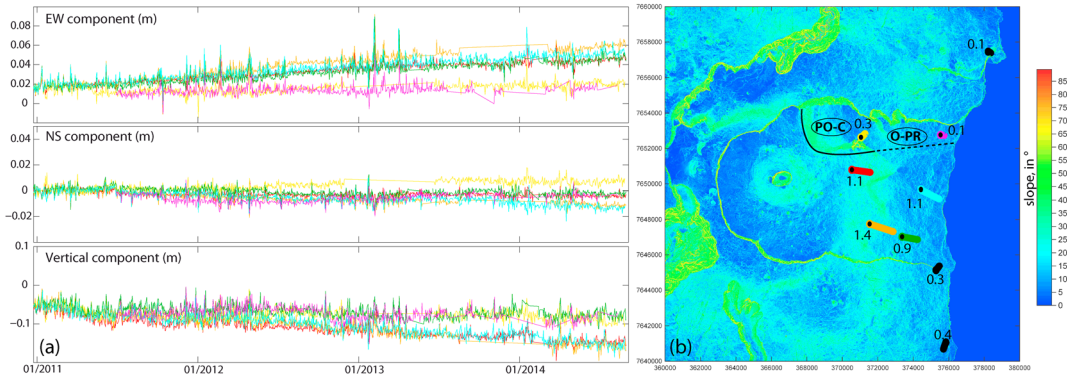


Figure 6. (a): Cumulated displacements (with plate motion removed) recorded on the EW, NS, and vertical components of the GNSS receivers implemented in the eastern flank (colors refer to the location of the GNSS on the map). (b): Slope (in degrees) of the volcano, with the horizontal displacement rates (in cm/yr) recorded in the eastern flank during 2011–2014. PO-C and OPR refer to Plaine des Osmondes Collapse and Osmondes Paleo-River, respectively (location after *Michon and Saint-Ange* [2008]).

for GPSG), whereas GBSG is installed on a 38 year old lava flow (emplaced in 1976). Thus, the subsidence recorded on these three stations could be linked to the still ongoing subsidence of the cooling lava flows on which they are installed, as observed at Etna [*Briole et al*., 1997] or on the 2007 huge lava flow at Piton de la Fournaise [*Servadio*, 2011]. Between 2010 and 2014, the EW displacement recorded on the GBSG station (installed on an old lava flow) is quite identical to the one recorded on the HDLG, GPSG, and GPNG stations (installed on younger lava flows) (Figure 6). This pattern tends to show that the measured EW displacements are not affected by the cooling of the lava flows on which the GNSS stations are installed. *Griffiths and Fink* [1993] and *Griffiths* [2000] showed that a solid crust quickly forms and grows at the surface of lava flows; from a certain thickness the flow only spreads in depth. Thus, the strength of the lava flow in the plane parallel to its surface is far greater than the strength in the plane transverse to its surface. Consequently, most of the lava flow consolidation on which the GNSS stations are installed occurs vertically between 2010 and 2014, and the viscous spreading of the lava flow parallel to its surface is negligible during this period. If such a slope-parallel viscous spreading occurred, it would be different from one station to the other according to the slope and the lava flow thickness, which is not observed on the HDLG, GBSG, GPNG, and GPSG stations, where similar EW displacements were recorded between 2010 and 2014 (Figures 6a and 6b).

The densification of the GNSS network on the eastern flank allows us to evidence that the EW extension observed on the cone flanks during rest periods (notably during 2011–2014) extends down to the steep Grandes Pentes area (Figure 3c). But the cause of the extension is distinct in each area: the extension of the cone flanks is controlled by the summit inward displacements, whereas the extension of the upper eastern flank is controlled by the eastward motion of the eastern flank (see the associated ground displacements in Figure 5d). Our strain maps (Figures 4b, 4d, 5b, and 5d) and the temporal trends (Figures 3c–3e, bottom) show that during rest periods contraction occurs in the steep southern Grandes Pentes area, i.e., the middle eastern flank and in the lower eastern flank. The EW contraction is clearly shown during the most recent period (2011–2014; Figure 5d) in the middle and lower eastern flank, whereas EW extension occurred in the upper eastern flank.

All GNSS stations were available only from the end of 2010 and recorded the last series of eruptions/intrusions (end 2010 to early 2011). This allowed us to depict the deformation pattern on the whole edifice down to the shore line. The 14 October 2010 eruptive fissures opened only 286 m southwest of the FOAG station and were responsible for the observed sharp decrease in strain in the EW direction (contraction) at the southeastern base of the cone (e.g., $\varepsilon_{xx} = \sim -7 \cdot 10^{-5}$ inside the FOAG, FERG, GPSG triangle; Figure 3c, bottom). After this eruption, the EW extension of the upper eastern flank and the EW contraction of the middle and lower eastern flanks increased (Figures 3c–3e, bottom). Indeed, an acceleration of the upper eastern flank motion to the east has been recorded by GPNG and GPSG during the eruptive/intrusive sequence spanning between October 2010 and February 2011 (3.1 cm/yr and 2.8 cm/yr, against 0.8 cm/yr and 1.1 cm/yr after February 2011 on GPNG and GPSG, respectively; Figures 3c and 3d, top). This led to a larger extension in the upper flank (areal dilation of

©2015. American Geophysical Union. All Rights Reserved.

$\sim 12 \cdot 10^{-6}$ from October 2010 to February 2011; Figure 3c, bottom) and a contraction in the middle flank during this period (areal dilation of $\sim -7 \cdot 10^{-7}$ from October 2010 to February 2011; Figure 3d, bottom). During this period, even if the lower eastern flank was less influenced by the volcano activity, it also recorded an acceleration of its contraction ($\sim -6 \cdot 10^{-6}$ strain per year from October 2010 to February 2011, against $\sim -3 \cdot 10^{-6}$ strain per year after early 2011; Figure 3e, bottom). All these accelerations stopped after the intrusion of 2 February 2011.

From February 2011 (the last intrusive episode shown in this study) to early 2014, the deformation trends on each area of the volcano were quite stable and display from the summit to the lower eastern flank (Figure 5d):

1. an EW contraction at the cone summit (e.g., $\varepsilon_{xx} = \sim -1 \times 10^{-4}$ in 3 years on Figure 3a);
2. an EW extension on the cone flank (e.g., $\varepsilon_{xx} = \sim 0.25 \times 10^{-4}$ in 3 years on Figure 3b);
3. an EW extension on the upper eastern flank (e.g., $\varepsilon_{xx} = \sim 1.2 \times 10^{-5}$ in 3 years; Figure 3c);
4. a limited EW contraction on the middle eastern flank (e.g., $\varepsilon_{xx} = \sim -0.6 \times 10^{-6}$ in 3 years on Figure 3d),
5. an EW contraction on the lower eastern flank (e.g., $\varepsilon_{xx} = \sim -2 \times 10^{-6}$ in 3 years; Figure 3e).

4. Discussion

4.1. Deformation Regime of the Volcano Terminal Cone—"Pulsation" of the Volcano and Fracturing

The Piton de la Fournaise terminal cone displays two main deformation regimes with antagonist patterns. Summit inflation during preeruptive/eruptive sequences (extension of the summit / contraction of the cone flanks) alternates with summit deflation during posteruptive/rest periods (contraction of the summit/extension of the cone flanks), and generates a "pulsation" (stress-strain cycles) of the volcano with an antagonist pattern between the summit and the base of the terminal cone (Figures 2, 3a, 3b, 4, and 5). The preeruptive summit inflation is linked to the pressurization of the shallow magma plumbing system, which extends inside the edifice from ~0.5 km to ~5 km below the surface [e.g., *Peltier et al*., 2009; *Prôno et al*., 2009; *Di Muro et al*., 2014], whereas the posteruptive summit deflation corresponds to the renewal of the edifice contraction/relaxation, which followed the April 2007 Dolomieu crater collapse [e.g., *Peltier et al*., 2010; *Staudacher and Peltier*, 2015]. At long term the summit subsidence is allowed by the eastern flank motion, which lowers the pressure of the magma storage system on which the cone is built [*Got et al*., 2013].

This volcano pulsation increases rock fracturing and damage, decreases the rock stiffness, and increases the medium permeability. It may be the cause of the intense fracturing affecting the terminal cone, evidenced by seismicity and geological observations [*Carter et al*., 2007].

During the preeruptive periods (weeks/months preceding an eruption), the seismicity rate accelerates (up to few hundred volcano-tectonic events per day) at Piton de la Fournaise (Figure 3a) [*Peltier et al*., 2009; *Schmid et al*., 2012; *Carrier et al*., 2015]. Seismicity shows that damage occurs into the edifice around the magma reservoir and up to the subsurface [e.g., *Prôno et al*., 2009; *Massin et al*., 2011]. *Carrier et al*. [2015] proposed a damage model to explain the weakening of the volcano edifice during the magma pressurization stages. Such progressive damage of the edifice would be at the origin of the preeruptive acceleration of seismicity and ground deformation. The summit extension preceding the renewal of eruptive activity are also consistent with other results derived from seismic data. Savage et al. (M. K. Savage et al., Seismic anisotropy and its precursory change before eruptions at Piton de la Fournaise volcano, La Réunion, submitted to *Journal of Geophysical Research*, 2015) evidence, from seismic shear wave splitting, that the time delay between the two components of the wave increases and that the fast direction rotates before eruptions. The time delay increase is consistent with the systematic seismic velocity reduction, detected by ambient seismic noise correlation, before eruptions and attributed to the increasing number of cracks in response to the preeruptive edifice inflation [e.g., *Brenguier et al*., 2008; *Rivet et al*., 2014].

During rest periods, the summit contraction and the extension at the base of the cone (Figures 4 and 5), would favor fracturing and increase of the permeability at the base of the cone, in the area where M. K. Savage et al. (submitted manuscript, 2015) detect low *Vp/Vs* seismic ratio during the same periods.

4.2. Deformation Regime of the Eastern Flank—Implication for the Relief of the Grandes Pentes Area

Our results show that the deformation regime of the eastern flank is influenced by the eruptive activity and is thus distinct during active and rest periods.

©2015. American Geophysical Union. All Rights Reserved.

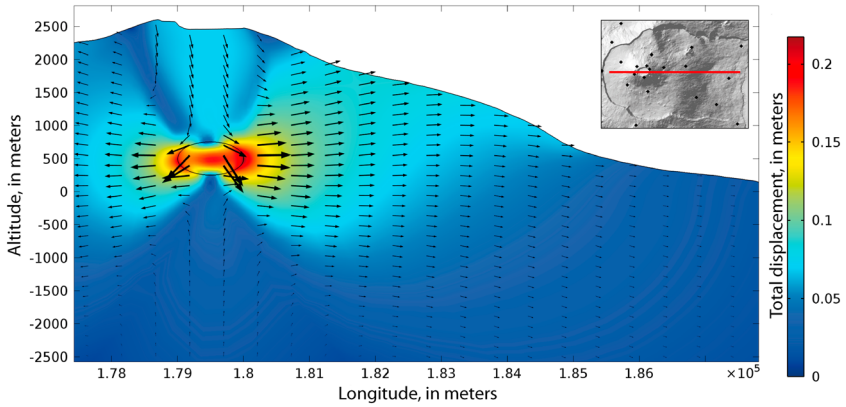


Figure 7. Two-dimensional (E-W cross section, see the location in the inset), numerical modeling of the displacements associated to a reservoir depressurization at Piton de la Fournaise. Magma reservoir is depressurized (underpressure: 3 MPa), so that the summit loads the reservoir and the eastern flank (elastoplastic medium, friction angle $\varphi = 25°$, cohesion $C = 1$ MPa, Young modulus = 50 GPa; these values have been chosen as they best fit the ground observations). Direction and amplitude of the displacements are given by the arrows and the color scale, respectively.

4.2.1. Periods of Preeruptive/Eruptive Summit Inflation

When the summit quickly inflates, the eastern flank contracts: the eastern flank resists to the load exerted by the pressurization of the shallow magma plumbing system. It behaves as an elastic or elastoplastic medium with a high internal friction angle (30°) [*Got et al*., 2013]. During these periods, stress accumulates in the edifice (Figures 3, bottom, 4a, 4c, 5a, and 5c). *Got et al*. [2013] showed that for the highly eruptive periods preceding the April 2007 summit collapse, the elastic stress was relaxed when plastic deformation occurred (i.e., when the plastic threshold was reached) leading to the large eastern flank stick-slip and distal eruptions. During such distal eruptions, the upper and middle eastern flanks uplifted (up to 37 cm in April 2007) [*Clarke et al*., 2013] and moved to the east (up to 1.4 m in April 2007) [*Clarke et al*., 2013]. Such large strains correspond to physically admissible stresses only when considering plastic or viscous deformation in the eastern flank, rather than purely elastic deformation. Since April 2007 no large distal event occurred again, but an acceleration of the upper eastern flank motion to the east has been recorded during the eruptive/intrusive sequence spanning between October 2010 and February 2011 (Figure 3c). Such a behavior of the eastern flank, with large displacements, is an evidence of mass transfer in depth from the summit to the east.

4.2.2. Periods of Posteruptive/Intereruptive Summit Deflation

Got et al. [2013] showed that for the period spanning 2004–2007, the plastic deformation of the upper eastern flank relaxed the elastic stress accumulated in and around the reservoir, the edifice was able to stabilize and to strengthen after a limited eastward displacement; a new stress cycle could restart.

Since then and the monitoring of the eastern flank by GNSS, we observe that during the post and intereruptive periods the upper and middle eastern flanks can no longer resist and spread to the east.

1. Whereas the summit of the cone subsides, the upper and middle eastern flanks steadily move to the east at constant rates (Figures 3c, 3d, and 5d):

   Summit subsidence is driven by gravity and magma pressure. Steady eastward displacement of the eastern flank occurs. In a perfectly elastic medium such a steady strain rate would imply a constant growth of the applied stress. However, rock strength is not infinite and rock elastic limit is necessarily reached. Such a steady deformation may therefore occur at constant stress during a plastic or viscoplastic deformation (Figure 7). This plastic deformation may eventually localize on an interface in the eastern flank; in this case the friction law along the interface controls the stress in the edifice. *Got et al*. [2013] showed that strain weakening occurred during rock rupture and associated eruptive magma transfer, with eventual localization of the plastic strain (internal friction angle of 15°; 15° is a low value for a volcano edifice and favors the idea of a decollement or a sill) along a subhorizontal structure that may be pressurized and form a sill [see also *Famin and Michon*, 2010; *Chaput et al*., 2014]. Note that the seismicity below the eastern flank is rare (about 10 per year during 2010–2014), far less

©2015. American Geophysical Union. All Rights Reserved.

than below the summit. It occurs between −2 to −4 km below sea level and does not occur in shallow swarms as observed at the summit. No subhorizontal seismic decollement plane has been evidenced in this area as it was performed at Kilauea [*Got et al*., 1994]. Therefore, the steady strain rate eastward displacement recorded in the eastern flank is realized mostly aseismically. *Carrier et al*. [2015] showed that, due to the high seismic rate below the summit and around the magma reservoir, damage occurred and magma reservoir pressure may be almost constant during tens of days during intereruptive and preeruptive periods. If the steady strain rate deformation of the eastern flank occurs at constant stress/reservoir pressure, eastern flank deformation is plastic and the volcanic system may be considered as "open": stress does not accumulate in the edifice. This steady state regime and constant rate correspond to an equilibrium between incoming magma pressure, reservoir pressure, cone weight, and flank strength. Unsteady strain rates could be due to the eventual time dependency in the friction law or in the applied stress if it is lower than the plastic threshold.

2. The lower eastern flank contracts (Figures 3e, bottom, 4d, and 5d).

   The lower eastern flank resists to the load of the upper structures (cone, upper and middle eastern flanks). Comparing the constant rate displacement of the middle eastern flank (Grandes Pentes) with the lower eastern flank contraction means that the lower eastern flank has a higher plasticity threshold than the Grandes Pentes area. The progressive loading of this lower part of the volcano may lead to the accumulation of elastic stress there.
   This area thus controls the stability of the entire eastern flank. As this lower part of the volcano has necessarily an elastoplastic behavior (its elastic deformation is limited), the future dynamics of the eastern flank depends on how this lower part can yield. For rock masses, yielding generally occurs by strain weakening, that is, rock strength decreases with strain. Lower eastern flank may yield with a limited weakening; in that case, stick-slip motion could occur, a limited slip inducing a sufficient drop in the loading stress and stabilization. It may yield with strong weakening and strain localization: in that case, large slip and acceleration could result before stabilization, which could lead to a catastrophic event. Therefore, accumulation of strain and elastic stress in this area of the eastern flank brings it closer to the instability, but the mode and magnitude of this instability depends on the (unknown) strain weakening law of this rock mass.

3. The relief of the Grandes Pentes area incrementally builds from mass accumulation, resulting to the contrast between the upper and medium eastern flanks plastic sliding and the lower eastern flank locking. This mass accumulation leads to the progressive stiffening of the Grandes Pentes area. This has to be linked to *Dieterich's* [1988] model, following which in such volcanoes, the topographic slope is controlled by the basal (or rock) friction: low (respectively strong) topographic slopes correspond to low (respectively strong) friction. This conclusion may be applied to each of the strain-determined domains: summit cone (no horizontal differential displacement of the summit cone relative to upper eastern flank, strong topographic slope), upper eastern flank (low slopes, low friction), middle eastern flank (Grandes Pentes, strong slopes, strong friction), and lower eastern flank. The extension of the steep slopes of the middle eastern flank (Grandes Pentes) (Figure 6b) tends to show that the conditions leading to its building exist for a long time. This also suggests that low friction, eventually due to a subhorizontal interface or a sill, could repeatedly exist for long periods below the upper eastern flank.

   As a summary, the long-term evolution of the middle-lower eastern flank due to horizontal differential displacement may lead to the following: (1) a (possibly catastrophic) eastward displacement of the lower eastern flank, (2) a middle eastern flank gravitational instability as observed at Hilina Pali (Hawaii) [e.g., *Denlinger and Okubo*, 1995], or (3) a thrust of the middle eastern flank above the lower eastern flank, following the respective strengths of the rock masses in each domain.

The deformation pattern described above does not concern the CRAG and GBNG stations located north of the Grandes Pentes/Grand Brulé areas. These two stations are located inside paleostructures (Figure 6b), i.e., Plaine des Osmondes collapse and Osmondes paleoriver [*Courteaud*, 1996; *Descloitres et al*., 1997; *Michon and Saint-Ange*, 2008]. These remaining structures are delimited by paleofractures that could explain the decoupling between these two stations (that recorded no significant displacement) and the four other stations implemented in the Grandes Pentes/Grand Brûlé areas.

©2015. American Geophysical Union. All Rights Reserved.

5. Conclusions

The study of the strain evolution and distribution derived from a dense GNSS network at Piton de la Fournaise allows us to investigate the volcano deformation patterns on the whole active part of the edifice. We evidenced the following:

1. a pulsation (stress-strain cycles) of the volcano with summit inflation during preeruptive/eruptive sequences (extension of the summit/contraction of the cone flanks) that alternates with summit deflation during posteruptive/rest periods (contraction of the summit/extension of the cone flanks);
2. mass transfer in depth from the summit to the east, realized at constant pressure through the plastic deformation of the eastern flank;
3. simultaneous extension and eastward displacement of the upper eastern flank and eastward contraction of the middle and lower eastern flanks that contribute to build the Grandes Pentes relief, steeping the topographic slope;
4. a mechanical decoupling between the northern and the middle/southern part of the Grandes Pentes/Grand Brûlé area;
5. a progressive loading of the lower eastern flank by the upper eastern flank, which brings the eastern flank closer to an eventual instability.

Appendix A: Chronogram of the Permanent GNSS Network Implementation

The permanent GNSS network maintained by the Volcanological Observatory of Piton de la Fournaise (Observatoire Volcanologique du Piton de la Fournaise) has been progressively installed since 2002 (Figure A1). The first stations have been installed around the summit craters with two reference stations located outside of the Enclos Fouqué caldera (GITG, ENCG), but their recording became continuous only from 2004. In 2005, the network has been completed by installing five more stations at the base of the terminal cone. After the major eruption of March–April 2007 and in the framework of the ANR UnderVolc project, five more stations have been installed in the Grandes Pentes and Grand Brûlé areas (CRAG, GPNG, GPSG, GBSG, and HDLG), i.e., the volcano eastern flank and two stations close to the coastline outside of the Enclos Fouqué caldera (CASG and TRCG). In 2011, the GBNG station in the northern Grand Brûlé has completed the coverage of the eastern flank.

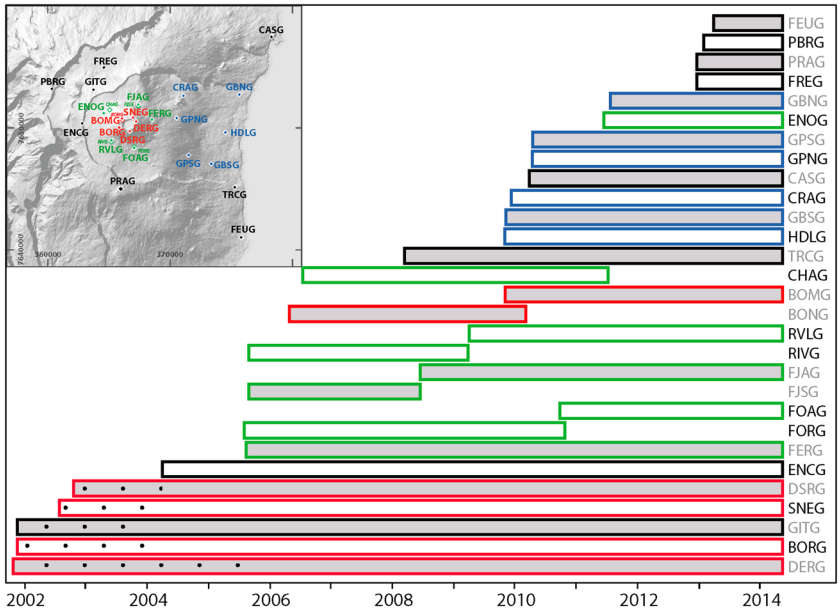


Figure A1. Chronogram of the permanent GNSS network implementation at Piton de la Fournaise volcano (in red: the summit stations, in green: the stations at the base of the terminal cone, in blue: the stations in the eastern flank, in black: the stations outside of the Enclos Fouqué caldera; see the inset for their location). The white diamonds surrounded by colored borders correspond to the dismantled stations (names with small font size). The dotted sections represent the period during which the stations were not permanent.

©2015. American Geophysical Union. All Rights Reserved.

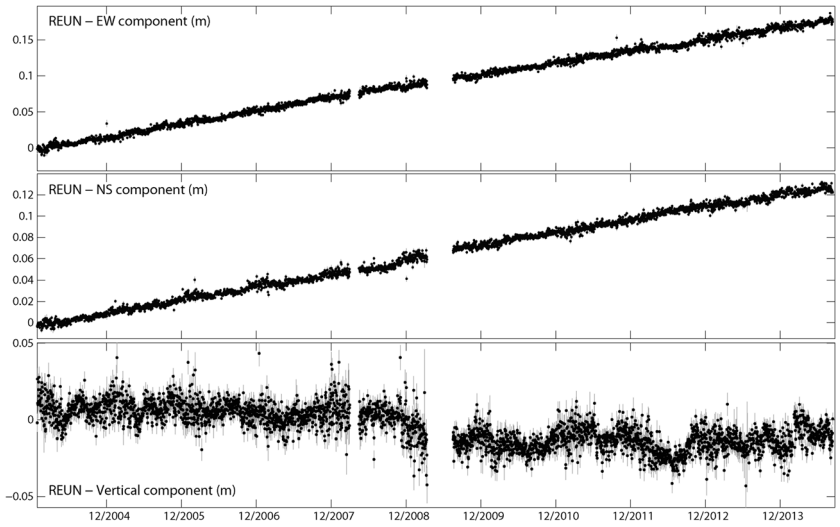


Figure B1. Cumulated displacements recorded on the REUN IGS GNSS receiver on the EW, NS, and vertical components over time.

In 2012–2013, the GNSS network has been enlarged by four stations (FREG, PRAG, PBRG, and FEUG) outside of the Enclos Fouqué caldera. This led to a good coverage of the whole edifice by the GNSS network.

Appendix B: REUN IGS Station Displacements

Data of the REUN IGS station have been used to correct our data from the plate motion. This station, located about 15 km west of the Piton de la Fournaise summit, is too far to record any displacement linked to the volcano activity and mainly records the effect of the plate motion. For each studied periods, we estimated the displacement velocity at REUN on the EW, NS, and vertical components, and we used them to detrend the recordings of the GNSS stations on the volcano, and thus to remove the displacement due to the plate motion. Figure B1 shows the trends recorded at REUN between 2004 and 2014 (i.e., the period covered by the OVPF permanent GNSS network).

Acknowledgments
The GNSS data used in this paper were collected by the Observatoire Volcanologique du Piton de la Fournaise/Institut de Physique du Globe de Paris (OVPF/IPGP). We are grateful to C. Brunet, P. Catherine, P. Kowalski, and F. Lauret for their help in maintaining the OVPF GNSS network in the field. Part of this work was supported by EMERGENCES 2011 grant from the city of Paris and by the ANR-08-RISK-011 (UNDERVOLC) project. We greatly appreciate the comments of the Associate Editor and two anonymous reviewers. This is IPGP contribution 3599.

References

Annen, C., J.-F. Lénat, and A. Provost (2001), The long-term growth of volcanic edifices: Numerical modeling of the role of dyke intrusion and lava-flow emplacement, *J. Volcanol. Geotherm. Res.*, *105*(4), 263–289.

Arnadottir, T., B. Lund, W. Jiang, H. Geirsson, H. Bjornsson, P. Einarsson, and T. Sigurdsson (2009), Glacial rebound and plate spreading: Results from the first countrywide GPS observations in Iceland, *Geophys. J. Int.*, *177*, 691–716.

Brenguier, F., N. M. Shapiro, M. Campillo, V. Ferrazzini, Z. Duputel, O. Coutant, and A. Nercessian (2008), Towards forecasting volcanic eruptions using seismic noise, *Nat. Geosci.*, *1*, 126–130.

Brenguier, F., et al. (2012), First results from the UnderVolc high resolution seismic and GPS network deployed on Piton de la Fournaise volcano, *Seismol. Res. Lett.*, *83*(7), 97–102, doi:10.1785/gssrl.83.1.97.

Briole, P., D. Massonet, and C. Delacourt (1997), Post-eruptive deformation associated with the 1986–87 and 1989 lava flows of Etnea detected by radar interferometry, *Geophys. Res. Lett.*, *24*(1), 37–40, doi:10.1029/96GL03705.

Carrier, A., J.-L. Got, A. Peltier, V. Ferrazzini, T. Staudacher, P. Kowalski, and P. Boissier (2015), A damage model for volcanic edifices: Implications for edifice strength, magma pressure, and eruptive processes, *J. Geophys. Res. Solid Earth*, *120*, 567–583, doi:10.1002/2014JB011485.

Carter, A., B. van Wyk, K. de Vries, P. B. Kelfoun, and P. Briole (2007), Pits, rifts and slumps: The summit structure of Piton de la Fournaise, *Bull. Volcanol.*, *69*, 741–756.

Chaput, M., V. Pinel, V. Famin, L. Michon, and F.-L. Froger (2014), Cointrusive shear displacement by sill intrusion in a detachment: A numerical approach, *Geophys. Res. Lett.*, *41*, 1937–1943, doi:10.1002/2013GL058813.

Clarke, D., F. Brenguier, J.-L. Froger, N. M. Shapiro, A. Peltier, and T. Staudacher (2013), Timing of a large volcanic flank movement at Piton de la Fournaise Volcano using noise-based seismic monitoring and ground deformation measurements, *Geophys. J. Int.*, *195*(2), 1132–1140.

Courteaud, M. (1996), Etudes des structures géologiques et hydrogéologiques du massif de La Fournaise par la méthode audiomagnétollurique, PhD thesis, Univ. de La Réunion, France, p. 212.

Denlinger, R. P., and P. Okubo (1995), Structure of the mobile south flank of Kilauea Volcano, Hawaii, *J. Geophys. Res.*, *100*(B12), 24,499–24,507, doi:10.1029/95JB01479.

Descloitres, M., M. Ritz, B. Robineau, and M. Courteaud (1997), Electrical structure beneath the eastern collapsed flank of Piton de la Fournaise volcano, Reunion Island: Implications for the quest for groundwater, *Water Resour. Res.*, *33*(1), 13–19, doi:10.1029/96WR02673.

Di Muro, A., N. Metrich, D. Vergani, M. Rosi, P. Armienti, T. Fougeroux, E. Deloule, I. Arienzo, and L. Civetta (2014), The shallow plumbing system of Piton de la Fournaise volcano (La Réunion Island, Indian Ocean) revealed by the major 2007 caldera-forming eruption, *J. Petrol.*, *55*(7), 1287–1315.

©2015. American Geophysical Union. All Rights Reserved.

Dieterich, J. H. (1988), Growth and persistence of Hawaiian volcanic rift zones, *J. Geophys. Res.*, *93*(B5), 4258–4270, doi:10.1029/JB093iB05p04258.
Famin, V., and L. Michon (2010), Volcano destabilization by magma injection in a detachment, *Geology*, *38*, 219–222.
Frank, F. C. (1966), Deduction of earth strains from survey data, *Bull. Seismol. Soc. Am.*, *56*, 35–42.
Got, J.-L., J. Fréchet, and F. W. Klein (1994), Deep fault plane geometry inferred from multiplet relative relocation beneath the south flank of Kilauea, *J. Geophys. Res.*, *99*, 15,375–15,386, doi:10.1029/94JB00577.
Got, J. L., A. Peltier, T. Staudacher, P. Kowalski, and P. Boissier (2013), Edifice strength and magma transfer modulation at Piton de la Fournaise volcano, *J. Geophys. Res. Solid Earth*, *118*, 1–18, doi:10.1002/jgrb.50350.
Griffiths, R. W. (2000), The dynamics of lava flows, *Annu. Rev. Fluid Mech.*, *32*, 477–518.
Griffiths, R. W., and J. H. Fink (1993), Effects of surface cooling on the spreading of lava flows and domes, *J. Fluid Mech.*, *252*, 667–702.
Hackl, M., R. Malservisi, and S. Wdowinski (2009), Strain rate patterns from dense GPS networks, *Nat. Hazards Earth Syst. Sci.*, *9*, 1177–1187.
Herring, T. A., R. W. King, and S. C. McClusky (2010), GPS analysis at MIT, Release 10.4, Massachusetts Institute of Technology, Cambridge.
Kahle, H.-G., M. Cocard, Y. Peter, A. Geiger, R. Reilinger, A. Barka, and G. Veis (2000), GPS-derived strain rate field within the boundary zones of the Eurasian, African, and Arabian Plates, *J. Geophys. Res.*, *105*, 23,353–23,370, doi:10.1029/2000JB900238.
Massin, F., V. Ferrazzini, P. Bachèlery, A. Nercessian, Z. Duputel, and T. Staudacher (2011), Structures and evolution of the plumbing system of Piton de la Fournaise volcano inferred from clustering of 2007 eruptive cycle seismicity, *J. Volcanol. Geotherm. Res.*, *202*, 96–106.
McGuire, W. J. (1996), Volcano instability: A review of contemporary theme, in *Volcano Instability on the Earth and Other Planets*, Geol. Soc. London Spec. Publ., vol. 110, edited by W. J. McGuire, A. P. Jones, and J. Neuberg, pp. 1–23.
Michon, L., and F. Saint-Ange (2008), Morphology of Piton de la Fournaise basaltic shield volcano (La Réunion Island): Characterization and implication in the volcano evolution, *J. Geophys. Res.*, *113*, B03203, doi:10.1029/2005JB004118.
Michon, L., T. Staudacher, V. Ferrazzini, P. Bachèlery, and J. Marti (2007), April 2007 collapse of Piton de La Fournaise: A new example of caldera formation, *Geophys. Res. Lett.*, *34*, L21301, doi:10.1029/2007GL031248.
Peltier, A., V. Famin, P. Bachèlery, V. Cayol, Y. Fukushima, and T. Staudacher (2008), Cyclic magma storages and transfers at Piton de La Fournaise volcano (La Réunion hotspot) inferred from deformation and geochemical data, *Earth Planet. Sci. Lett.*, *270*, 180–188.
Peltier, A., P. Bachèlery, and T. Staudacher (2009), Magma transfer and storage at Piton de La Fournaise (La Réunion Island) between 1972 and 2007: A review of geophysical and geochemical data, *J. Volcanol. Geotherm. Res.*, *184*(1–2), 93–108.
Peltier, A., T. Staudacher, and P. Bachèlery (2010), New behaviour of the Piton de la Fournaise volcano feeding system (La Réunion Island) deduced from GPS data: Influence of the 2007 Dolomieu caldera collapse, *J. Volcanol. Geotherm. Res.*, *192*, 48–56.
Peltier, A., M. Poland, and T. Staudacher (2015), Are Piton de la Fournaise (La Réunion) and Kīlauea (Hawai'i) really "analog volcanoes"?, in *Hawaiian Volcanoes: From Source to Surface*, *AGU Monogr.*, vol. 208, pp. 507–531, John Wiley, Hoboken, N. J. [Available at http://eu.wiley.com/WileyCDA/WileyTitle/productCd-1118872045.html.]
Prôno, E., J. Battaglia, V. Monteiller, J. L. Got, and V. Ferrazzini (2009), P-wave velocity structure of Piton de la Fournaise volcano deduced from seismic data recorded between 1996 and 1999, *J. Volcanol. Geotherm. Res.*, *184*(1–2), 49–62.
Rivet, D., F. Brenguier, D. Clarke, N. M. Shapiro, and A. Peltier (2014), Long-term dynamics of Piton de la Fournaise volcano from 13 years of seismic velocity change measurements and GPS observations, *J. Geophys. Res. Solid Earth*, *119*, 7654–7666, doi:10.1002/2014JB011307.
Roult, G., A. Peltier, B. Taisne, T. Staudacher, V. Ferrazzini, A. Di Muro, and the OVPF group (2012), A new comprehensive classification of the Piton de la Fournaise eruptions spanning the 1986–2011 period. Search and analysis of eruption precursors from a broad-band seismological station, *J. Volcanol. Geotherm. Res.*, *241–242*, 78–104.
Schmid, A., J.-R. Grasso, D. Clarke, V. Ferrazzini, P. Bachèlery, and T. Staudacher (2012), Eruption forerunners from multiparameter monitoring and application for eruptions time predictability (Piton de la Fournaise), *J. Geophys. Res.*, *117*, B11203, doi:10.1029/2012JB009167.
Servadio, Z. (2011), Apports de l'imagerie à haute resolution spectral et spatial dans les bilans de volume et les bilans radiatifs au Piton de La Fournaise, PhD thesis, Univ. of La Réunion, France, p. 312.
Staudacher, T., and A. Peltier (2015), Ground deformation at Piton de la Fournaise (La Réunion Island), a review from 20 years of GNSS monitoring, in *Active Volcanoes of the Southwest Indian Ocean: Piton de la Fournaise and Karthala. Active Volcanoes of the World*, edited by P. Bachèlery et al., Springer, Berlin.
Staudacher, T., V. Ferrazzini, A. Peltier, P. Kowalski, P. Boissier, P. Catherine, F. Lauret, and F. Massin (2009), The April 2007 eruption and the Dolomieu crater collapse, two major events at Piton de la Fournaise, *J. Volcanol. Geotherm. Res.*, *184*(1–2), 126–137.
Takahashi, H. (2011), Static strain and stress changes in eastern Japan due to the 2011 off the Pacific coast of Tohoku Earthquake, as derived from GPS data, *Earth Planets Space*, *63*, 741–744.
Walker, G. P. L. (1986), Koolau dyke complex, Oahu: Intensity and origin of a sheeted-dyke complex high in a Hawaiian volcanic edifice, *Geology*, *14*, 310–313.

©2015. American Geophysical Union. All Rights Reserved.